



On the chain-melted phase of matter

Victor Naden Robinson^{a,1}, Hongxiang Zong^{b,1,2}, Graeme J. Ackland^a, Gavin Woolman^a, and Andreas Hermann^{a,2}

^aCentre for Science at Extreme Conditions and School of Physics and Astronomy, University of Edinburgh, Edinburgh EH9 3FD, United Kingdom; and ^bState Key Laboratory for Mechanical Behavior of Materials, Xi'an Jiantong University, Xi'an, Shanxi 710049, China

Edited by Erio Tosatti, International School for Advanced Studies, and CNR-IOM Democritos, Trieste, Italy; and International Centre for Theoretical Physics, Trieste, Italy, and approved March 14, 2019 (received for review January 17, 2019)

Various single elements form incommensurate crystal structures under pressure, where a zeolite-type “host” sublattice surrounds a “guest” sublattice comprising 1D chains of atoms. On “chain melting,” diffraction peaks from the guest sublattice vanish, while those from the host remain. Diffusion of the guest atoms is expected to be confined to the channels in the host sublattice, which suggests 1D melting. Here, we present atomistic simulations of potassium to investigate this phenomenon and demonstrate that the chain-melted phase has no long-ranged order either along or between the chains. This 3D disorder provides the extensive entropy necessary to make the chain melt a true thermodynamic phase of matter, yet with the unique property that diffusion remains confined to 1D only. Calculations necessitated the development of an interatomic forcefield using machine learning, which we show fully reproduces potassium’s phase diagram, including the chain-melted state and 14 known phase transitions.

potassium | high pressure | incommensurate | chain melting | machine learning

Melting can be defined in many ways: inability to sustain shear, disappearance of long-range order, internal flow of particles, or transition to a condensed state with lower free energy than any crystal. The molten state can coexist with the solid, normally by spatial separation, but in some unusual states of matter, interpenetration of two macroscopic components occurs, creating a single phase. Superfluid He is one example, with a Bose condensate coexisting with “normal” liquid. Another example is the superionic state (1–4), where the lighter sublattice of a solid loses long-range order and diffuses freely in three dimensions like a charged liquid, while the heavier sublattice remains crystalline. In the high-pressure phases of many metals, a subset of certain Bragg peaks disappear on heating: a phenomenon described as “chain melting,” the inverted commas indicating ongoing uncertainty as to whether this is a transition to another new phase of matter (5–7); a similar phenomenon is seen in some compounds at ambient pressure (8, 9).

The elemental phases that show this behavior are incommensurate host–guest (HG) structures—perhaps the most striking manifestation of the alkali elements’ departure from the simple metal picture under compression (5, 10–22), and also seen in various other elements under pressure (23–27). HG structures (see Fig. 1) consist of two sublattices with 1D atomic “guest” chains located in channels within a zeolite-type “host” structure. They have been observed for sodium (>125 GPa), potassium (20 GPa), and rubidium (17 GPa), with further complex phases appearing at higher pressure. The host structure is identical in all three, but the guest lattices are different: sodium’s is monoclinic, whereas potassium’s and rubidium’s are tetragonal, with different symmetries. Common features of HG structures are the formation of relatively large crystals through recrystallization and a drop in reflectivity (14, 28, 29).

When HG structures are heated, diffraction peaks from the guest sublattice can disappear, the signature of chain melting. The conventional melting line also has a minimum around the pressures where the HG and other electrified phases (with valence

electrons localized in interstitial space) exist. Exactly how the atoms move in the chain-melted phase is unclear. The diffraction data could be explained by chains losing long-range 1D order along their length, by 2D disorder with chains sliding independently along the *c* direction, by 3D disorder with both these processes occurring, or even by superionic diffusion of the former guest atoms between chains in 3D.

Although the chain melting has been described as low-dimensional (6), potassium occupies all three dimensions, so the thermodynamic situation is different from 1D and 2D model systems. Purely 2D melting (30, 31), such as the XY model or 1D transitions, which tend to be nonequilibrium (32), balance energy and entropy, which are both extensive. For the HG structures, however, if only correlation between chains is lost, the per-atom energy cost will always outweigh the per-chain entropic term in the thermodynamic limit. Similarly, if order is only lost along chains, the 3D per-atom energy cost will outweigh the 1D entropy. So the chain melt can only be a thermodynamic phase of matter if order is lost both along and between chains simultaneously. This cannot be unambiguously determined from the loss of diffraction peaks, and accurate calorimetry is impossible at these temperatures and pressures.

Thus, it remains unclear whether the chain-melted phase is thermodynamically stable. In this work, we address this issue by using a variety of simulation methods to investigate the

Significance

Several elements form host–guest structures under pressure. Upon heating, the guest atoms can “melt,” while the host atoms remain crystalline. In this partially molten state, the “molten” guest atoms remain confined to 1D channels, which suggests thermodynamically impossible 1D melting. The complicated crystal structures, with incommensurate ratios between host and guest atoms, prohibit simulations with electronic structure methods. We develop here a classical interatomic forcefield for the element potassium using machine-learning techniques and simulate the chain-melted state with up to 20,000 atoms. We show that in the chain-melted state, guest-atom correlations are lost in three dimensions, providing the entropy necessary for its thermodynamic stability.

Author contributions: G.J.A. and A.H. designed research; V.N.R., H.Z., and G.W. performed research; H.Z. contributed new reagents/analytic tools; V.N.R., H.Z., G.J.A., G.W., and A.H. analyzed data; and V.N.R., H.Z., G.J.A., G.W., and A.H. wrote the paper.

The authors declare no conflict of interest.

This article is a PNAS Direct Submission.

Published under the PNAS license.

Data deposition: Data reported in this paper have been deposited on The University of Edinburgh repository, <https://datashare.is.ed.ac.uk/handle/10283/3300>.

¹V.N.R. and H.Z. contributed equally to this work.

²To whom correspondence may be addressed. Email: a.hermann@ed.ac.uk or zonghust@mail.xjtu.edu.

This article contains supporting information online at www.pnas.org/lookup/suppl/doi:10.1073/pnas.1900985116/-DCSupplemental.

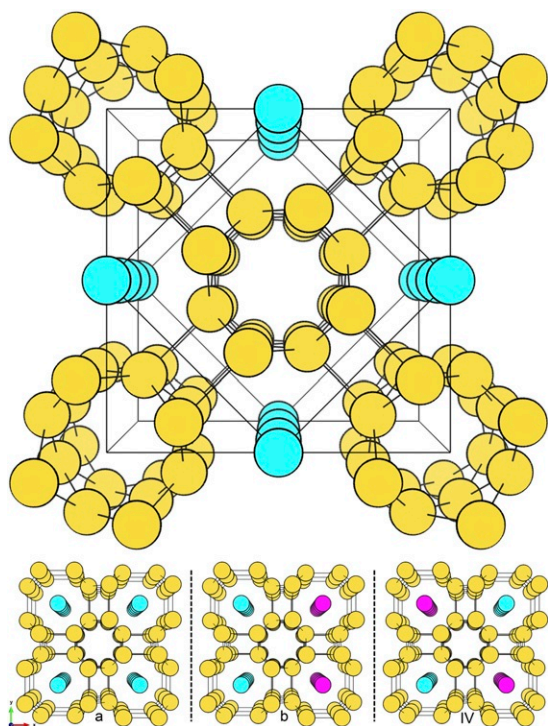


Fig. 1. (Upper) Top view of the incommensurate HG structure K-III. Yellow (cyan) spheres denote the host (guest) atoms. (Lower) Guest symmetries for the IIIa, IIIb, and Rb-IV structures labeled a, b, and IV, respectively. Cyan (purple) guest atoms are at $z = 0$ ($z = c_g/2$).

dimensionality of chain melting in the HG phases with respect to the atomic motion, correlation, and disorder. The nontrivial electronic structure of the HG phases, with their partial electride nature, suggests that first-principles descriptions are required. These, however, severely limit the size of the melting simulations. To overcome the finite size effects, we use machine learning to train a classical atomic interaction potential, which we then use to study the chain-melted state, but which also describes the rest of potassium's phase diagram very well. Recent developments in X-ray diagnostics of dynamic compression experiments allow confirmation of HG phase formation on the nanosecond time scale; (7) atomistic simulations of the shock propagation through such a material rely on a potential that is transferrable across all relevant phases (33–37).

Potassium as an Exemplar System

In diamond anvil cell experiments, potassium under compression transforms, like other simple metals, from body-centered cubic (BCC) to face-centered cubic (FCC). Above 19 GPa, these simple structures become unstable against highly complex structures. The first of these, K-III, is the HG phase. At higher pressures, potassium transforms further to a sequence of electride structures (17, 38). The HG structure K-III itself has two phase transformations ($K\text{-IIIa} \rightarrow K\text{-IIIb} \rightarrow K\text{-IIIa}$) within the guest structure alone (19). Potassium enters the tetragonal K-IIIa structure at 20 GPa at room temperature, with all guest chains perfectly aligned along the c axis, forming the simplest of the HG structures. At 30 GPa, K-IIIa transforms to K-IIIb, where every other chain along the a axis is shifted by half the guest atom spacing, in a striped formation, thus doubling the guest unit cell. A related structure, Rb-IV, shifts the chains in a checkerboard fashion, also doubling the unit cell. Fig. 1 sketches the chain alignments in the different structures. At 38 GPa, the K-IIIa structure reenters the

phase diagram and at 54 GPa K-III is succeeded by the $oP8$ structure (38).

At room temperature, the relative guest-chain positions are well correlated throughout the crystal, evidenced by the diffraction spots for the guest structures IIIa and IIIb. Upon heating, the guest X-ray diffraction peaks have been observed to become diffuse (6), signaling a loss of long-range order. The loss of the guest diffraction peaks has been mapped out experimentally on heating and cooling and associated with so-called chain melting where the interchain position becomes uncorrelated. However, the atomic-level nature of the higher-temperature phase is not fully understood. The full melt line for the HG structure has also not yet been determined either in experiment or calculation.

The ground-state energetics of potassium's phases is well described by density functional theory (DFT). The delicate features of the K-III phases in particular have been discussed in detail recently (22), with the incommensurability treated by interpolation between rational approximant models for the HG axial ratio. The energetics showed incommensurate HG c -axis ratios c_h/c_g between 1.60 and 1.67 for the most stable forms of the HG structure and reproduced its pressure dependence, including a turnover of the HG axial ratio and the reentrant stability of K-IIIa (19). Static calculations imply that at intermediate pressures, the Rb-IV structure, and not K-IIIb, is most stable. However, including vibrational zero-point energies and entropies within the harmonic approximation reverses their energetic order and stabilizes K-IIIb, in agreement with the experimental situation (see *SI Appendix* for details).

This work provides a suitable starting point for molecular-dynamics (MD) simulations, with a particular focus on phase transitions in the HG structure's sublattices. However, although

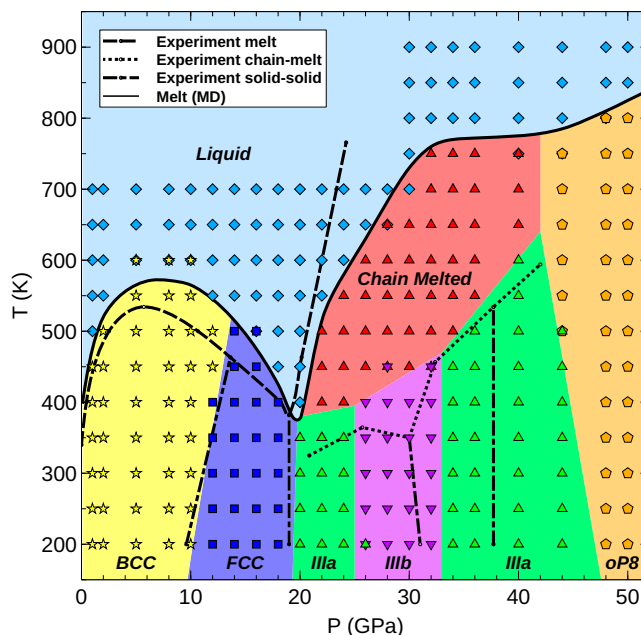


Fig. 2. Forcefield simulated phase diagram of potassium. Each datapoint represents an MLMD NVT calculation initialized in the shown phase at 200 K and the corresponding DFT density and then heated. Symbols distinguish the various phases: Each simulation was repeated several times, and double symbols indicate where the final phase was ambiguous. Colored regions refer to the simulated region of stability for each phase; a solid black line is the melting line obtained from the simulations. Chain melting was determined by the loss of correlation between chains (text). Experimental phase boundaries for melting (dashed line), chain-melting (dotted), and solid–solid phase transitions (dash-dotted) are taken from ref. 6.

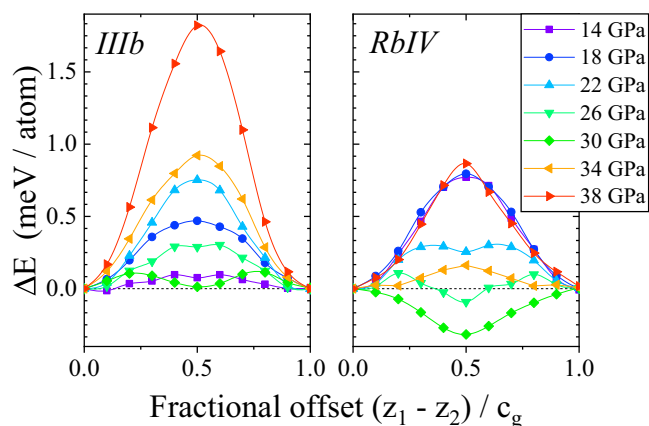


Fig. 3. DFT potential energy surface for sliding adjacent guest chains in K-III, anchored at z_1 and z_2 , respectively, by one unit of c_g , in appropriately doubled unit cells. Both the transitions from K-IIIa to the stripe pattern of K-IIIb and the checkerboard pattern of Rb-IV were calculated—these structures correspond to relative displacements $(z_1 - z_2)/c_g$ of 0.5, while K-IIIa corresponds to 0.0 or 1.0. For incommensurate structures, the actual value of z_1 is irrelevant. The forcefield model produces similar results.

DFT describes the energetics correctly, it is too computationally demanding to reliably study long-range correlations, longer timescales, and thermodynamic phase stability. These challenges can be overcome with model forcefields of sufficient accuracy. Since HG phases appear at high pressures and temperatures, the demands on the forcefield are considerable: to capture the full phase diagram of potassium up to 60 GPa, reproducing phase stabilities (of phases with quite different electronic characters), phase transitions, HG chain dynamics and melting, and the melt line. However, these are all structural transitions defined by the atomic positions, and so an interatomic forcefield is well suited for this task. We therefore first produced a set of ab-initio MD (AIMD) trajectories in the constant number of particles, volume, and temperature (NVT) ensemble up to $P \approx 60$ GPa and $T = 1,500$ K—see the [SI Appendix](#) for details of the calculations and the resulting phase diagram. We then used this database to develop a machine-learned interatomic forcefield (Methods and [SI Appendix](#)). This allowed for machine-learned MD (MLMD) with fully converged statistics (39). The forcefield was validated by using MLMD in the NVT ensemble to calculate the (P, T) phase diagram of potassium up to 50 GPa and 1,000 K. The agreement with experiment, including all observed phases and the melting-curve maximum and minimum (40), is remarkable (Fig. 2).

Between 0 and 20 GPa, we use the forcefield to find the solid–solid phase transition between BCC and FCC, by starting from FCC and heating in MD. The model also reproduces the melting line’s distinct features, with a maximum and subsequent minimum, at very similar pressures to those seen in experiment, and slightly higher temperatures. Such slight superheating is typical of our method of heat-until-it-melts.

Above 20 GPa, the K-IIIa phase is stable and the melting line steeply increases, in line with experimental data. Single-phase simulations started in FCC or K-IIIa remained in their initial structure, indicating that this transformation is kinetically difficult; however, the phase boundary can be mapped by using phase-coexistence calculations.

Between 20 and 44 GPa, the simulations found either the K-IIIa or -IIIb structure at low temperatures, although the IIIa→IIIb→IIIa transition pressures (26, 34 GPa) are slightly lower than seen in the room-temperature experiment (30, 38 GPa). This pressure difference is also observed in static DFT (22) and may represent experimental hysteresis since the exper-

iments were done by increasing pressure. Curiously, the AIMD simulations in the intermediate-pressure range (28 GPa in particular) settle into the Rb-IV guest structure, likely due to finite size effects and limited simulation time, whereas the MLMD simulations, trained on these AIMD data, instead produce the K-IIIb structure—in agreement with experiment and vibrational entropy considerations. At higher temperatures, simulations starting in IIIa or IIIb exhibit chain melting, closely following the experimental situation. It is possible that varying the HG ratio may alter this transition pressure and chain-melting temperature. Further heating produces a fully molten liquid at ~ 780 K at 36 GPa. The initially very steep melting line of K-III flattens out considerably at pressures >32 GPa, so much so that our data cannot rule out a second melting maximum, before the melting line of the *oP8* structure increases again.

Above 40 GPa, simulations settled in the stable phase of IIIa or *oP8*, with a transition pressure between the two at ~ 45 GPa at $T = 300$ K. The direct transformation between IIIa and *oP8* was observed in MLMD. This is again slightly lower than the experimental pressure of between 50 and 55 GPa (41) and higher than the static calculation result of 39 GPa; however, the simulated data achieve the correct Clapeyron slope, calculated from the latent heat and volume differences in the ground state.

The guest-structure transitions can be probed by sliding adjacent guest chains against each other to produce the K-IIIa, -IIIb, or Rb-IV structures. Fig. 3 shows the energy cost (or gain) involved in transforming IIIa to either IIIb or Rb-IV, and back, as determined from DFT. This shows that the K-IIIa structure is preferred at both low and high pressures. The Rb-IV structure becomes favored at ~ 25 GPa and remains thus until ~ 33 GPa. The K-IIIb structure, meanwhile, is almost energetically degenerate with K-IIIa at ~ 30 GPa. If chain melting were related to loss of order between chains only, the chain-melting temperature should correlate with the energy barriers shown in Fig. 3. In particular, chain melting should happen at very low temperatures at ~ 26 – 30 GPa, where the energy cost to slide chains against each other almost vanishes. This is not what is seen in experiment or in our calculations, and we will explore the nature of the chain-melted phase in more detail now.

The Chain-Melted Phase

We simulated the HG phase with MD using both AIMD and MLMD forces, with a particular focus on flow and decorrelation within the guest structure. At low temperatures, guest chains are ordered with a certain pressure-dependent symmetry (IIIa and IIIb). However, the guest lattices in K-III are incommensurate with the host, so they should be able to move relative to the host lattice with no energy penalty, producing a zero-frequency phonon mode (42). In Fig. 4, we show that, even at 200 K, well below the chain-melting temperature at 40 GPa, the guest atoms do indeed slide freely along the c direction. However, both host and guest structures remain solid; the guest lattice in particular

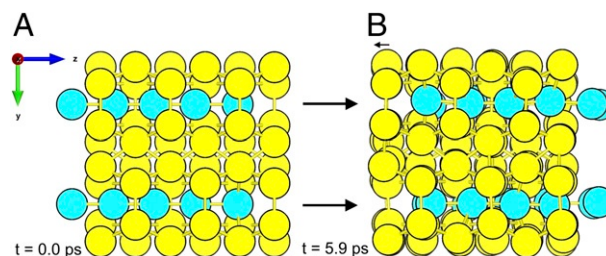


Fig. 4. Side view of K-IIIa at 40 GPa and $T = 200$ K. (A) The initial AIMD setup. (B) The final positions after 5.9 ps.

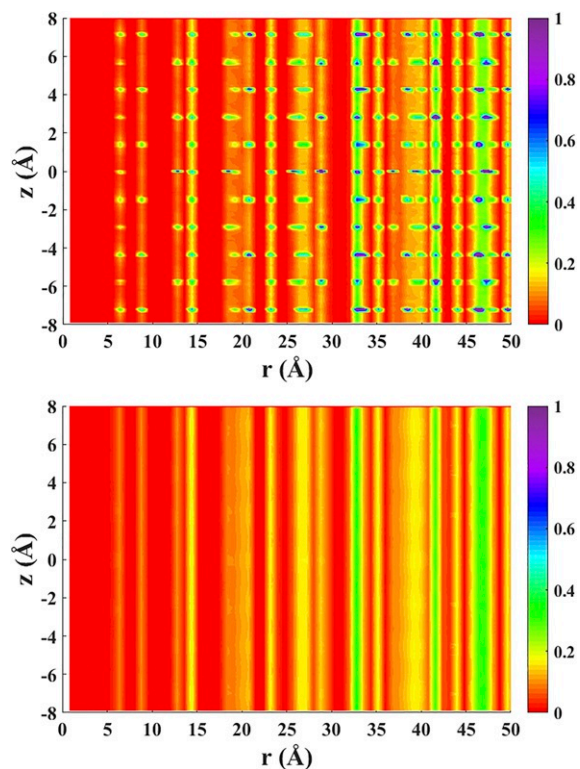


Fig. 5. Normalized chain-correlation function $\sigma_{xy}(r, z)$ from MLMD simulations at 28 GPa, for the solid at $T = 200$ K (Upper) and the chain melt at 500 K (Lower), where r and z refer to separation in the xy plane and along the z axis, respectively. See legends on the sides for color scheme, which ranges from $\sigma_{xy} = 0$ (red) to $\sigma_{xy} = 1$ (purple). The solid has well-defined peaks and thus long-range order both in-plane and along the chains; the peak pattern has the signature of K-IIIb (compare *SI Appendix, Table S2* and *Fig. S3*).

retains intrachain and interchain correlations (see also [Movie S1](#)). A standard measure of melting, the mean squared displacement of atoms, already diverges well below the chain-melting transition, and to discern between K-IIIa, -IIIb, and Rb-IV, we define spatial-correlation functions along chains, $\sigma_z(z)$, and between chains, $\sigma_{xy}(r, z)$; see Methods for details.

For a solid guest lattice, both σ_z and σ_{xy} should show long-range order along z and perpendicular, along r . Above the chain-melting transition, σ_{xy} will detect loss of order between chains and σ_z loss of order along chains. Moreover, $\sigma_{xy}(r, z)$ can distinguish between the solid K-IIIa phase on one hand (where peaks appear at $z = n \cdot c_g$) and the K-IIIb or Rb-IV structure on the other hand [where peaks are also at $z = (n + \frac{1}{2})c_g$].

In *Fig. 5*, we show $\sigma_{xy}(r, z)$ from MLMD simulations at 28 GPa and two different temperatures. At 200 K, the guest structure is solid, and the peak positions in σ_{xy} are consistent with the K-IIIb structure (see *SI Appendix* for simulations of σ_{xy} for the different guest structures). At 500 K, the peaks along z have vanished, indicating loss of correlation between guest chains. Lines along r remain, as chain atoms remain confined to their respective host channels.

In *Fig. 6*, we show the radially integrated correlation function $\langle \sigma_{xy}(z) \rangle = \int_0^\infty \sigma_{xy}(r, z) dr$ at 22, 28, and 40 GPa, and the intrachain correlation function $\sigma_z(z)$ at 40 GPa. The former illustrates how the chain melt can be clearly seen in the loss of interchain correlation. For σ_z , any practical ab-initio simulation shows order throughout the supercell. However, the MLMD simulation allowed us to simulate chains of lengths up to 100 atoms.

Fig. 6 shows long-range oscillatory order for σ_z at low temperatures, but exponentially decaying short-range order above the chain-melting temperature. This shows that, in the chain-melted state, there is short-ranged order along the chains with a range greater than any ab-initio supercell size, and also much longer than the interchain correlation length, but that the long-range behavior is uncorrelated disorder. The simulations have a fixed number of atoms per chain, but a variable number would only enhance the disorder.

One characteristic of a normal liquid is the loss of shear rigidity. In MD, this can be measured from the stress-strain relation, from stress fluctuations, or from strain fluctuations. In the chain-melted phase, the first two methods give the combined rigidity of the host and guest; however, strain can be defined and measured independently on each sublattice. We find divergent strain fluctuations, as measured by mean-squared atomic displacement in the z direction. The shear rigidity within the guest lattice is lost, but only along the z direction. Thus, atoms can flow freely through the chain melt, but only in one direction.

Conclusions

We investigated chain melting in potassium as an exemplar for other chain-melted materials and for behavior of other HG materials under pressure. We demonstrate that the chain melt is a novel phase of matter. The chain-melt phase is unlike a normal liquid since one sublattice remains ordered. It is unlike superionic matter because of the unique property that, while liquid-like

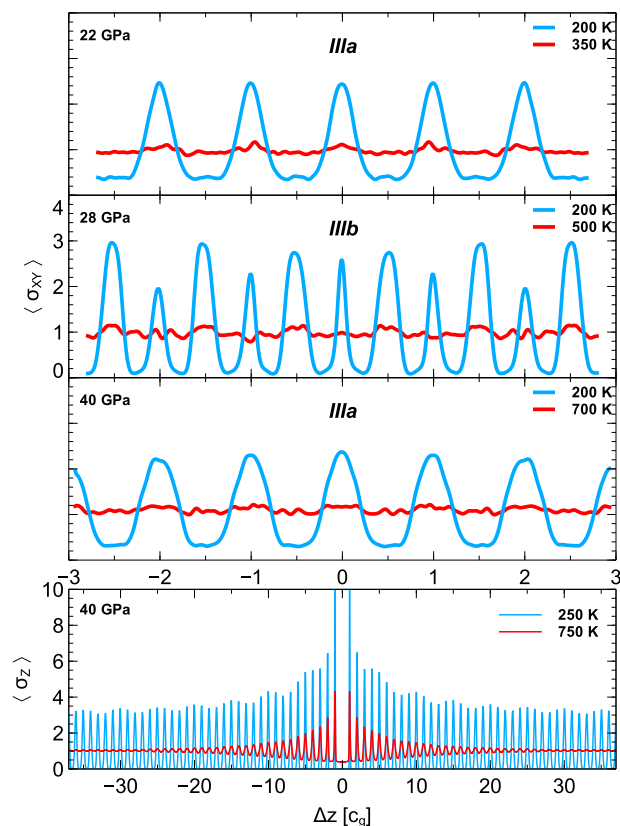


Fig. 6. (Upper) Interchain correlation $\langle \sigma_{xy}(z) \rangle$ at various T and P . Phase IIIa is indicated by peaks at integer multiples of c_g . Phase IIIb (or Rb-IV) has additional peaks at half-integer values. The chain melt has no peaks in the correlation function. (Lower) Correlation $\sigma_z(z)$ along the chains, showing long-range oscillatory order at 250 K (blue) and exponentially decaying short-ranged order at 750 K (red).

atomic diffusion occurs, exchange of particles between chains is impossible.

The phase diagram of potassium was investigated up to 60 GPa and 1,000 K by using AIMD and MLMD methods. As expected, the ab-initio results reproduce the experimental low-temperature stability and for the incommensurate HG phase showed free motion and disordering of the guest chains in 2D in small cells at finite temperature. The classical forcefield has only atomic degrees of freedom, while the electrified phases have non-atom-centered electrons. Nevertheless, the forcefield was also able to describe the entire phase diagram, including multiple phases, melting, and chain melting across the entire relevant phase space. Moreover, it enabled large enough simulations, which proved the intrachain disorder and thus the thermodynamic stability of the chain-melt phase.

The agreement with known experimental phase behavior means that the simulations can reliably extend the existing experimental data. They suggest a considerable flattening of potassium's melting line at high pressure about the HG phases and a transformation from K-IIIb to the Rb-IV structure at low temperature. The MLMD simulations enabled us to eliminate finite size effects and to detect diffusion and loss of long-range order of periodicity in any direction in the chain-melt phase. We have thus proved that the chain melt involves fully 3D disorder of the guest sublattice and is therefore a true thermodynamic phase and a unique state of matter.

Methods

DFT calculations used the CASTEP code (43). We used generalized-gradient approximated exchange correlation (44) and a nine-electron ultrasoft pseudopotential with 1.7-Å inner-core radius and 400-eV plane wave cutoff with k points sampled at the Γ point only in AIMD and with a grid density of 0.02 \AA^{-1} in structure optimization.

Constrained Guest-Structure Optimizations. The calculations of the guest-lattice potential energy surface involve energy minimization under the constraint of fixing the positions of two guest atoms in neighboring chains at z_1 and z_2 . We then varied the offset ($\delta: 0 \rightarrow 1 = (z_1 - z_2)/c_g$) relaxing all other (host and guest) atoms for each value of δ .

AIMD. Simulations ran at fixed density with a Nose-Hoover thermostat, using up to 192 atoms for K-IIIa with a 0.75-fs timestep, Berendsen equilibration for 1 ps, and up to 10-ps sampling. To simulate the entire (P, T) phase space, AIMD simulations of potassium were performed by using 128-atom supercells for BCC (1, 3, and 6 GPa), 108-atom FCC (9 and 12 GPa), 116-atom K-III using a 15 h-9 g (1.67) approximant (20, 22, 24, 40, and 50 GPa) and 8 h-5 g (1.60) approximant at 28 GPa, and 96-atom oP8 (40, 44, 50, and 56 GPa). AIMDs were run from $T = 200 \text{ K}$ in steps of at most 200 K up to $T = 1,500 \text{ K}$.

Machine Learning the Forces. In practice, interatomic forcefields are based on some functional form appropriate to the bonding, which may vary from phase to phase. This makes it very unusual for a single forcefield to correctly describe multiple phases. Here, the forcefield is trained by using the AIMD forces from four phases and atom-centered symmetry function descriptors (or fingerprints) of the local chemical environment (45, 46). Three types of descriptors are used: pairwise, three body, and local density.

- Boyce JB, Huberman BA (1979) Superionic conductors: Transitions, structures, dynamics. *Phys Rep* 51:189–265.
- Chau R, Mitchell AC, Minich RW, Nellis WJ (2001) Electrical conductivity of water compressed dynamically to pressures of 70–180 GPa (0.7–1.8 Mbar). *J Chem Phys* 114:1361–1365.
- Sugimura E, et al. (2012) Experimental evidence of superionic conduction in H₂O ice. *J Chem Phys* 137:194505.
- Millot M, et al. (2018) Experimental evidence for superionic water ice using shock compression. *Nat Phys* 14:297–302.
- McMahon MI, Nelmes RJ (2004) Chain “melting” in the composite Rb-IV structure. *Phys Rev Lett* 93:055501.
- McBride EE, et al. (2015) One-dimensional chain melting in incommensurate potassium. *Phys Rev B* 91:144111.

These descriptors are mapped into the corresponding atomic forces with the kernel ridge regression (KRR) method, capable of handling complex nonlinear relationships (47). KRR works on the principle of similarity, wherein the μ component of the atomic force on atom i is given by an average over the reference configurations (t), weighted by their similarity to i . We use a Gaussian kernel

$$F_i^\mu = \sum_t \alpha_t \cdot e^{-\frac{\|V_i^\mu - V_t^\mu\|}{2\sigma^2}}, \quad [1]$$

where t labels each reference atomic environment and V_t^μ is its corresponding fingerprint. α_t and σ are the weight coefficients and length-scale parameter, respectively. The optimal values for α_t and σ are determined during a training process involving cross-validation and regularization methods, using the full set of AIMD data. The forcefield (Eq. 1) was then integrated into the LAMMPS code (48) for the MLMD simulations.

MLMD. The simulations were performed by using periodic boundary conditions and a time step of 1 fs. To reproduce the entire temperature–pressure phase diagram, the MLMD simulations of K were conducted by including 16,000-atom supercells for BCC (1–10 GPa), 16,384-atom FCC (12–20 GPa), 1,536-atom K-III using a 15 h-9 g (1.67) approximant (20–24 and 34–44 GPa) and 8 h-5 g (1.60) at 26–32 GPa, and 360-atom oP8 (44–50 GPa) and were run from $T = 200 \text{ K}$ to $T = 900 \text{ K}$.

As for the correlation-function calculation, the interchain correlation ($\langle \sigma_{xy} \rangle$) was calculated based on 1,536-atom K-III supercells; the intrachain correlation σ_z at 40 GPa (Fig. 6) used 2,320-atom supercells with two chains; and the 2D chain correlation function σ_{xy} at 28 GPa (Fig. 5) was obtained from a supercell with 20,736 atoms and 144 chains.

For each simulation, the K sample was generated at the appropriate density and held at selected temperatures with NVT annealing for up to 50,000 steps.

The chain structure can be monitored by using the chain correlation functions $\sigma_z(z)$ and $\sigma_{xy}(r, z)$.

$$\sigma_z(\Delta z) \equiv \left\langle \sum_n \sum_{i \neq j} \delta(z_{ni} - z_{nj} - \Delta z) \right\rangle,$$

is the correlation function between the z coordinates of atoms within the same chain (n numbers the chain in the simulation box, and i, j atoms within the n -th chain). Likewise,

$$\sigma_{xy}(\Delta r, \Delta z) \equiv \left\langle \sum_{n \neq m} \sum_{i, j} \delta(z_{ni} - z_{mj} - \Delta z) \delta \left(\sqrt{(x_{ni} - x_{mj})^2 + (y_{ni} - y_{mj})^2} - \Delta r \right) \right\rangle,$$

is the correlation function between atoms in different chains: n and m are indices of the chains, and i and j label the guest atoms within the n -th and m -th chain.

Acknowledgments. V.N.R. and G.W. were supported by UK Engineering and Physical Sciences Research Council (EPSRC) Scottish Doctoral Training Centre in Condensed Matter Physics studentships. H.Z. and G.J.A. were supported by the European Research Council Project Hydrogen at Extreme Conditions: Applying Theory to Experiment for Creation, Verification and Understanding (HECATE) for funding. For computational support, we thank the UK national high-performance computing service, ARCHER, and the UK Materials and Molecular Modeling Hub, which is partially funded by EPSRC Grant EP/P020194, access for both of which was obtained via the UK Car-Parrinello Consortium and funded by EPSRC Grant EP/P022561/1.

- Briggs R, et al. (2017) Ultrafast X-ray diffraction Studies of the phase transitions and equation of state of scandium shock compressed to 82 GPa. *Phys Rev Lett* 118:025501.
- Hastings JM, et al. (1977) One-dimensional phonons and “phase-ordering” phase Transition in Hg_{2- δ} AsF₆. *Phys Rev Lett* 39:1484–1487.
- Wörle M, Nesper R, Chatterji TK (2006) LiB_x (0.82 < x < 1.0)—An incommensurate composite structure below 150 K. *Z Anorg Allg Chem* 632:1737–1742.
- Schwarz U, Grzechnik A, Syassen K, Loa I, Hanfland M (1999) Rubidium-IV: A high pressure phase with complex crystal structure. *Phys Rev Lett* 83:4085–4088.
- McMahon MI, Rekihi S, Nelmes RJ (2001) Pressure dependent incommensuration in Rb-IV. *Phys Rev Lett* 87:055501.
- Falconi S, et al. (2006) X-ray diffraction study of diffuse scattering in incommensurate rubidium-IV. *Phys Rev B* 73:214102.

13. McMahon MI, Nelmes RJ, Schwarz U, Syassen K (2006) Composite incommensurate K-III and a commensurate form: Study of a high-pressure phase of Potassium. *Phys Rev B* 74:140102.
14. Lundegaard LF, et al. (2009) Single-crystal Studies of incommensurate Na to 1.5 Mbar. *Phys Rev B* 79:064105.
15. Lazicki A, et al. (2009) Anomalous optical and electronic properties of dense sodium. *Proc Natl Acad Sci USA* 106:6525–6528.
16. Ma Y, et al. (2009) Transparent dense sodium. *Nature* 458:182–185.
17. Marqués M, et al. (2009) Potassium under pressure: A pseudobinary ionic compound. *Phys Rev Lett* 103:115501.
18. Marqués M, et al. (2011) Optical and electronic properties of dense sodium. *Phys Rev B* 83:184106.
19. Lundegaard LF, et al. (2013) Observation of a reentrant phase transition in incommensurate potassium. *Phys Rev B* 88:054106.
20. Loa I, et al. (2011) Plasmons in sodium under pressure: Increasing departure from nearly free-electron behavior. *Phys Rev Lett* 107:086402.
21. Marqués M, et al. (2011) Crystal structures of dense lithium: A metal-semiconductor-metal transition. *Phys Rev Lett* 106:095502.
22. Woolman G, et al. (2018) Structural and electronic properties of the alkali metal incommensurate phases. *Phys Rev Mater* 2:053604.
23. Nelmes RJ, Allan DR, McMahon MI, Belmonte SA (1999) Self-hosting incommensurate structure of barium IV. *Phys Rev Lett* 83:4081–4084.
24. McMahon MI, Degtyareva O, Nelmes RJ (2000) Ba-IV-Type incommensurate crystal structure in group-V metals. *Phys Rev Lett* 85:4896–4899.
25. McMahon MI, Bovornratanaraks T, Allan DR, Belmonte SA, Nelmes RJ (2000) Observation of the incommensurate barium-IV structure in strontium phase V. *Phys Rev B* 61:3135–3138.
26. Fujihisa H, et al. (2013) Ca-VII: A chain ordered host-guest structure of calcium above 210GPa. *Phys Rev Lett* 110:235501.
27. McMahon MI, Ackland GJ (2010) Aluminium: Simple metal no more. *Nat Mater* 9:607–608.
28. Takemura K, Syassen K (1983) High-pressure phase transitions in potassium and phase relations among heavy alkali metals. *Phys Rev B* 28:1193–1196.
29. Takemura K, Syassen K (1982) High pressure equation of state of rubidium. *Solid State Commun* 44:1161–1164.
30. Halperin BI, Nelson DR (1978) Theory of two-dimensional melting. *Phys Rev Lett* 41:121–124.
31. Strandburg KJ (1988) Two-dimensional melting. *Rev Mod Phys* 60:161–207.
32. Evans MR (2000) Phase transitions in one-dimensional nonequilibrium systems. *Braz J Phys* 30:42–57.
33. Bringa EM, et al. (2005) Ultrahigh strength in nanocrystalline materials under shock loading. *Science* 309:1838–1841.
34. Kadau K, et al. (2007) Shock waves in polycrystalline iron. *Phys Rev Lett* 98:135701.
35. Bartók AP, Payne MC, Kondor R, Csányi G (2010) Gaussian approximation potentials: The accuracy of quantum mechanics, without the electrons. *Phys Rev Lett* 104:136403.
36. Deringer VL, Csányi G (2017) Machine learning based interatomic potential for amorphous carbon. *Phys Rev B* 95:094203.
37. Zong H, Piliava G, Ding X (2018) Developing an interatomic potential for martensitic phase transformations in zirconium by machine learning. *npj Comput Mater* 4:48.
38. Lundegaard LF, et al. (2009) Observation of the oP8 crystal structure in potassium at high pressure. *Phys Rev B* 80:020101.
39. Behler J, Parrinello M (2007) Generalized neural-network representation of high-dimensional potential-energy surfaces. *Phys Rev Lett* 98:146401.
40. Narygina O, McBride E, Stinton G, McMahon M (2011) Melting curve of potassium to 22 GPa. *Phys Rev B* 84:054111.
41. Sakata M, Nakamoto Y, Matsuoka T, Ohishi Y, Shimizu K (2017) Structural phase transition of potassium under high-pressure and low-temperature condition. *J Phys Conf Ser* 950:042020.
42. Brown P, et al. (2018) Strong coupling superconductivity in a quasiperiodic host-guest structure. *Sci Adv* 4:eaa04793.
43. Clark SJ, et al. (2005) First principles methods using CASTEP. *Z Kristall* 220:567–570.
44. Perdew JP, Burke K, Ernzerhof M (1996) Generalized gradient approximation made simple. *Phys Rev Lett* 77:3865–3868.
45. Behler J (2014) Representing potential energy surfaces by high-dimensional neural network potentials. *J Phys Condens Matter* 26:183001.
46. Botu V, Ramprasad R (2015) Learning scheme to predict atomic forces and accelerate materials simulations. *Phys Rev B* 92:094306.
47. Kung SY (2014) *Kernel Methods and Machine Learning* (Cambridge Univ Press, Cambridge, UK).
48. Plimpton S (1995) Fast parallel algorithms for short-range molecular dynamics. *J Comput Phys* 117:1–19.